

Gap type effect on photocatalytic degradation using newly hydrotalcite nanoposite precursor synthesized by hydrothermal method

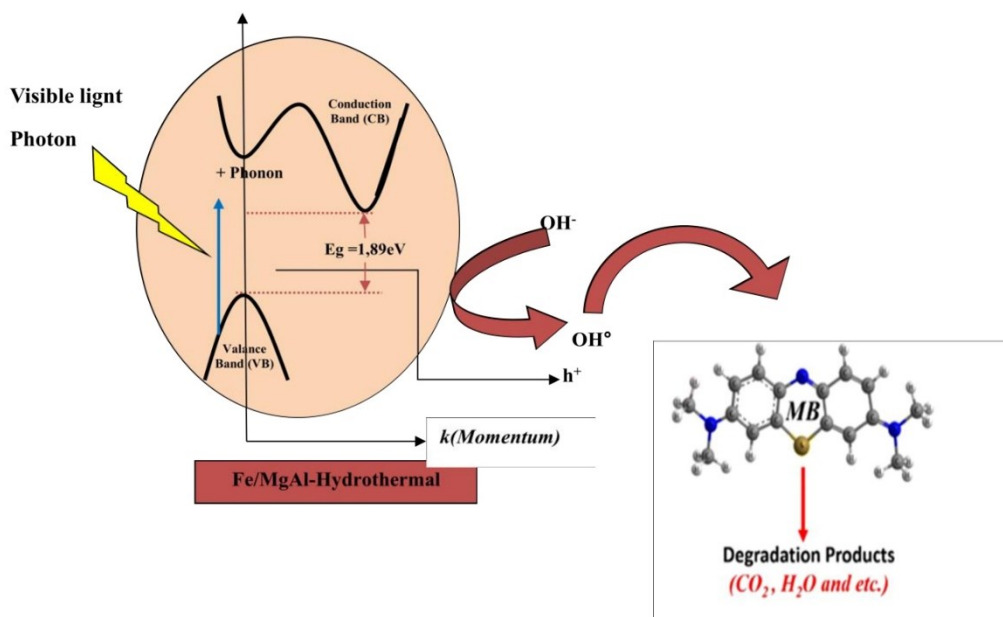
Souad Kerchich¹, Amel Boudjemaa², Redouane Chebout², Yacine Kerchich³, Imane Béchohra^{1*}, Khaldoun Bachari²

¹Laboratoire de Génie de la réaction, Faculté de Génie mécanique et de Génie des procédés-Université des sciences et de la technologie Houari Boumediene (USTHB), B.P. 32, El Alia, Bab Ezzouar, 16111, Alger, Algérie.

²Centre De Recherche Scientifique Et Technique En Analyses Physico-Chimique (CRAPC), BP 384, Siège ex-Pasna Zone Industrielle, Bou-Ismaïl CP 42004, Tipaza, Algérie.

³Laboratoire des sciences et techniques de l'environnement, Ecole nationale polytechnique, BP 182, El Harrach, Alger, Algérie.

GRAPHICAL ABSTRACT



ABSTRACT

A novel technique involving hydrothermal synthesis was employed to prepare nanocomposite precursors of lamellar double hydroxide based basic mixed oxides. This method extended ongoing research on iron-impregnated hydrotalcite-supported nanomaterials. The iron-based Fe/MgAl-h nanocomposite was prepared via dry impregnation, introducing a known % by weight of Fe (NO₃)₃·9H₂O metal salt into the hydrothermally synthesized MgAl-h structure. For comparative analysis, the photocatalytic performance of Fe/MgAl-h was compared with the coprecipitation-

20 synthesized Fe/MgAl-c after calcination at 400°C, using various characterization techniques.
21 Structural examination revealed a double-layered hydroxyl structure and the presence of iron oxide
22 phase Fe₂O₃ in Fe/MgAl-h400. Optical assessments indicated an indirect band gap energy of 1.89
23 eV for solid Fe/MgAl-h400, which is suitable for visible light absorption. Photocatalytic
24 experiments for methylene blue (MB) dye degradation in aqueous solution were performed under
25 artificial irradiation with a tungsten lamp as the visible light source, mirroring the conditions of
26 Fe/MgAl-c400. Using 50 mg/L MB concentration and 0.5 g/L catalyst quantity, increased MB
27 removal efficiency with time was observed. A comparative study of hydrothermal and
28 coprecipitation synthesis methods showed decreased photodegradation for the hydrothermally
29 prepared solid. Fe/MgAl-h400 and Fe/MgAl-c400 exhibited reaction efficiencies of approximately
30 46% and 67%, respectively, possibly attributed to their distinct indirect and direct band gap
31 characteristics. Moreover, a wider band gap in a semiconductor material offers several advantages
32 for the degradation of dyes.

33 **Keywords:** band gap, comparison, hydrothermal, co-precipitation, hydrotalcite, nanomaterials and
34 photocatalysis.

36 **Introduction**

37 Layered double hydroxides, also known as anionic clays or hydrotalcite-like compounds, are indeed
38 a class of solid basic catalysts that have offer a promising platform for the development of
39 environmentally friendly and efficient catalytic processes in the production of fine chemicals and
40 other chemical transformations. Researchers continue to explore and optimize their properties for
41 various applications in green chemistry and sustainable chemical synthesis.

42 hydrotalcites represent a category of both man-made and naturally occurring inorganic solids. These
43 materials consist of two-dimensional layered structures composed of positively charged layers

44 resembling brucite (Mg(OH)₂). Within these layers, you'll find bivalent and trivalent metal ions
45 arranged in an octahedral configuration (ALLMANN & HP, 1969; Taylor, 1973; Terzis *et al.*, 1987;
46 Pengfei *et al.*, 2020).

47 The hydrotalcite's general formula, denoted as $[M_{1-x}^{2+}M_x^{3+}(OH)_2]^{x+}[A_{x/n}^{n-} mH_2O]^x$, encompasses
48 various metal cations, represented by "M," including both divalent (e.g., Mg²⁺, Zn²⁺, Ni²⁺, Co²⁺,
49 Ca²⁺ etc.) and trivalent (e.g., Al³⁺, Fe³⁺, Cr³⁺, Mo³⁺, Co³⁺, Ga³⁺ etc.) species. Additionally, "A"
50 represents the intercalated anions. These hydrotalcite layers maintain electrical neutrality by
51 balancing their positive charge with the presence of negatively charged interlayer anions (Mishra *et*
52 *al.*, 2018b).

53 hydrotalcites, characterized by affordability, ready accessibility, and straightforward synthesis, have
54 emerged as highly promising options for a range of applications. This is due to their extensive
55 surface area, abundant surface-active sites, and impressive capacity for anion exchange, allowing
56 them to incorporate anions of various sizes and types within their layers. With the significant
57 attention hydrotalcites have garnered in recent years, a diverse array of hydrotalcite-based materials
58 has been developed through specialized techniques or the incorporation of various metal cations to
59 fulfill specific objectives (Fan *et al.*, 2014; Peng *et al.*, 2014; Patel *et al.*, 2017; Arrabito *et al.*,
60 2019; Yan *et al.*, 2019; Ameena Shirin *et al.*, 2021).

61 Over the past few decades, there has been a significant surge in interest surrounding the
62 development of nanoparticle-scale technology for a wide range of applications. As a result, various
63 synthesis techniques have emerged, encompassing gas phase, liquid phase, two-phase, sol-gel
64 methods, co-precipitation, and hydrothermal methods (Miyata & Kumura, 1973; Reichle, 1985;
65 Cavani *et al.*, 1991; Sels *et al.*, 2001). In this study, we aim to compare two prominent methods,
66 namely the co-precipitation method, which involves maintaining both constant and variable pH
67 levels (Crepaldi *et al.*, 2000), and the hydrothermal method (Reichle, 1986). It's worth noting that
68 hydrothermal synthesis can be combined with co-precipitation to enhance the crystallization of

69 hydrotalcite, a process with distinct advantages and limitations. Additionally, it's important to
70 recognize that the synthesis method employed significantly influences the structure of LDH, with
71 co-precipitation being a widely utilized approach in the production of hydrotalcite materials.

72 The precipitation at constant pH is generally applied to synthesize the hydrotalcites structure. The
73 synthesis is carried out by the addition of the solution of two different metal salts dissolved in the
74 distilled water. Which is added drop wise over an aqueous solution containing the mixture of anion
75 to be intercalated and NaOH to accelerate coprecipitation reaction in the pH range .The reaction is
76 carried out at room temperature (RT). The precipitate is then filtered and washed several times with
77 distilled water. The drying temperature is not allowed to exceed 120 °C (Terzis *et al.*, 1987). The
78 use of this method leads to obtaining of pure and homogenous hydrotalcite with a high crystallinity.

79 The advantage obtained by the co-precipitation at constant pH lies on the textural properties of the
80 hydrotalcites materials. The hydrotalcites structure prepared by this method bears a small particle
81 size, a high specific surface area and a high average pore diameter than the materials prepared at
82 variable pH (Faour *et al.*, 2010; Qin *et al.*, 2020). On the other hand, the co-precipitation method
83 allows to finely tuning the structure of the synthesized materials by controlling the MII/MIII molar
84 ratios, type of interlayer anion, the synthesis time, temperature, and the pH (Thevenot *et al.*, 1989;
85 Zhao *et al.*, 2003; Kloprogge *et al.*, 2004; Klemkaite *et al.*, 2011).

86 The hydrothermal synthesis is the combination with co-precipitation method to improve
87 hydrotalcite crystallization, were consists of the treatment of fresh precipitate of co-precipitation
88 synthesis resulting of mixing the solution containing metal salts and alkaline solution. The mixtures
89 are usually put inside a Teflon-lined autoclave in the temperatures range from 80 to 350°C and the
90 reaction times varied from hours to days (Miyata, 1980). The advantages of this method include its
91 simplicity and transformation of small crystallites of hydrotalcite into larger ones (Cavalcanti *et al.*,
92 1987). The Mg-Al prepared by this method had hexagonally shaped crystallites with a lateral
93 dimension of 1-3 μm (Xu & Lu, 2005). This technique is recommended to prepare mixed metal

94 oxides from hydrotalcite precursor (Xu & Lu, 2005; Jing *et al.*, 2010), ternary hydrotalcites systems
95 and inorganic/organic hybrid hydrotalcite (Carja *et al.*, 2008; Mishra *et al.*, 2018a).

96 Recently, research on hydrotalcite has been directed towards the development of new hybrid or
97 composite systems with improved physicochemical properties. The lamellar structures, in spite of
98 their remarkable basic properties (Fan *et al.*, 2014; Patel *et al.*, 2017; Mishra *et al.*, 2018b), are less
99 used in catalytic reactions than the mixed oxides, which are easier to process and exhibit higher
100 specific surface areas. Therefore, it will be very useful to adapt the basic properties of mixed oxides
101 obtained from hydrotalcite precursors which will be synthesized by important methods like
102 coprecipitation and hydrothermal method in order to carry out reactions requiring different basic
103 resistances.

104 Numerous hydrotalcite supported nanoparticles, two-dimensional graphene oxide sheets or metal
105 complexes have already proven to be very effective towards catalysis, photocatalysis, adsorption,
106 sensing and biological applications (Choudary *et al.*, 2002; Garcia-Gallastegui *et al.*, 2012; Islam *et*
107 *al.*, 2015, 2019; Allou *et al.*, 2017; Asif *et al.*, 2017). Also, it is noteworthy that iron Oxide
108 Nanoparticles supported on clays exhibit many interesting properties that can be used in a variety of
109 applications (Oliveira *et al.*, 2003; Nishio *et al.*, 2007; da Silva *et al.*, 2010; Chen *et al.*, 2017;
110 Kerchich *et al.*, 2021).

111 In this article, Kerchich *et al.* (2021) (Kerchich *et al.*, 2021), conducted a study aiming to provide a
112 systematic overview and a concise comparison between hydrothermal synthesis and co-precipitation
113 methods. The research also includes a structural analysis and explores the potential application of
114 Fe/MgAl in photocatalysis for the purpose of removing methylene blue dye.

115

116 **Experimental section**

117 **Synthetic methods of semiconductor nanoparticles**

118 **Preparation of MgAl-h support by hydrothermal method**

119 The MgAl support was prepared using two distinct methods. In the first method, known as the
120 hydrothermal method, the reaction involved the addition of appropriate quantities of Mg
121 $(\text{NO}_3)_2 \cdot 6\text{H}_2\text{O}$ (0.2 M, Aldrich, 99%), $\text{Al}(\text{NO}_3)_3 \cdot 6\text{H}_2\text{O}$ (0.1 M, Aldrich, 99.1%), and NaOH (2 M,
122 Aldrich, 99%) to achieve a constant pH of approximately 12. A laboratory pH meter (Hanna HI
123 2211) was employed to control the addition of the alkaline solution. The resulting mixture was
124 placed inside a Teflon-lined autoclave and maintained at a temperature of 80°C for 17 hours
125 (overnight). Subsequently, the formed gel underwent a washing process using distilled water and
126 was finally dried overnight (Chebout et al., 2010; Kerchiche, Chebout, & Bachari, 2017; Riman,
127 Suchanek, & Lencka, 2002).

128 On the other hand, in the coprecipitation method used to synthesize MgAl-c material with the same
129 Mg/Al, the initial step paralleled the hydrothermal method, involving the addition of the specified
130 amounts of Mg $(\text{NO}_3)_2 \cdot 6\text{H}_2\text{O}$ (0.2 M, Aldrich, 99%), $\text{Al}(\text{NO}_3)_3 \cdot 6\text{H}_2\text{O}$ (0.1 M, Aldrich, 99.1%), and
131 NaOH (2 M, Aldrich, 99%) to maintain a constant pH of around 12. The subsequent step diverged
132 as the mixture was transferred to a balloon heater under nitrogen reflux, with the temperature
133 maintained at 70°C for 18 hours to achieve a pure, well-crystallized compound. The final product
134 was obtained after washing/centrifugation with bidistilled water and subsequent drying in an oven
135 at 80°C for 12 hours (Riman *et al.*, 2002; Chebout *et al.*, 2010; Kerchiche *et al.*, 2017). Finally, both
136 based HDL materials underwent a crushing and sieving process to achieve a fine particle size before
137 before appropriate use. The host material resulting from the hydrothermal method was denoted as
138 MgAl-LDHh, while the material synthesized through coprecipitation was designated as MgAl-
139 LDHc.

140 **Preparation of nanocomposite $\text{Fe}_2\text{O}_3/\text{MgAl-h}$**

141 The protocol for preparing the Fe/MgAl solid by impregnation consists in bringing the MgAl
142 support into contact with an iron content of a known % by weight of the metal precursor, the metal
143 salt $\text{Fe}(\text{NO}_3)_3 \cdot 9\text{H}_2\text{O}$ (Aldrich, 97%). For this work, the choice is focused on the dry impregnation

144 method to prepare the Fe/ MgAl materials. The volume of the metal salt solution which must
145 correspond to the volume of the pores of the support. This method is limited by the solubility of the
146 precursor metal and is used to prepare catalysts with weak interactions between the metal and the
147 support (Desportes *et al.*, 2005). The mixture is then stirred for 2 hours by magnetic stirring and the
148 excess solution is removed by evaporation then by drying in an oven overnight at 80 °C and
149 calcined at 400 °C for 4 hours. The materials were denoted Fe/MgAl-h and Fe/MgAlc for
150 hydrothermal and coprecipitation method respectively.

151 **Characterization techniques**

152 Diffuse reflectance infrared Fourier-transform (DRIFT) spectra of the samples were obtained using
153 a Perkin-Elmer FTIR 1000 spectrometer, covering the wavelength range from 400 to 4000 cm⁻¹.
154 The chemical composition of the materials was determined using a Rigaku “ZSX Primus II” X-Ray
155 Fluorescence Spectrometer. Thermogravimetric (TGA) and differential thermal analysis (DTA)
156 were conducted using a Thermal Analyzer (Model SDT Q 600-TA) instrument. The sample
157 underwent heating from ambient temperature to 900 °C under N₂ flow, with a heating rate of 10 °C
158 min⁻¹. X-ray powder diffraction (XRD) patterns were recorded utilizing a Bruker D8 Advance X-
159 ray diffractometer, employing Cu K α 1 radiation ($\lambda\alpha = 1.54184 \text{ \AA}$, 40 kV, and 50 mA). The data
160 were collected within the 7° to 80° 2 θ range. The structural characteristics of the materials were
161 observed through scanning electron microscopy (SEM) using a FEI Quanta200 microscope
162 operating at 20 kV. UV–vis diffuse reflectance (DRS) spectra were recorded using a Shimadzu
163 model UV-2100 spectrophotometer equipped with an integrating sphere accessory, with BaSO₄
164 serving as the reference material. The obtained reflectance (R%) from the DRS spectrum was
165 utilized to determine the E_g value. The resulting solution was subject to analysis via atomic
166 absorption spectroscopy (240-FS Fast Sequential, AA range from Agilent).

167 **Photocatalytic reactivity study**

168 To investigate the photocatalytic degradation of the dye, we followed a specific experimental

169 procedure. This involved preparing a solution with a fixed concentration of the methylene blue
170 (MB) and a known quantity of synthetic material. We conducted these experiments in a 500 mL
171 Pyrex photochemical reactor with a double-wall design to maintain a constant temperature of 25°C,
172 achieved by employing a temperature-controlled bath. The light source used for irradiation was a
173 200 W tungsten lamp emitting light in the range of 400–800 nm, with an intensity of 2.10×10^{19}
174 photons per second. After the photocatalytic reaction, the suspension was subjected to
175 centrifugation at 3000 rpm for 10 minutes. Subsequently, we filtered the suspension to eliminate
176 any catalyst particles before performing absorbance measurements. To quantitatively assess the
177 results, we measured the absorbance at the wavelength $\lambda_{\text{max}} = 665$ nm using a Varian UV–visible
178 Spectrophotometer (Cary 50 UV–vis Spectrophotometer).

179 **Results and discussion**

180 **Structure and composition**

181 All the synthesized hydrotalcites exhibited two-step decomposition upon heating under air (Fig. 1).
182 Initially, the first step was observed at temperatures ranging from 220 to 250 °C, resulting in a 15%
183 reduction in weight. This initial weight loss corresponded to the removal of interlamellar water
184 molecules (Riman *et al.*, 2002; Desportes *et al.*, 2005; Kerchiche *et al.*, 2017; Ramos-Ramírez *et*
185 *al.*, 2020). Subsequently, in the temperature range between 250 and 600 °C, a weight loss of
186 approximately 25% and 35% was observed for MgAl-h and Fe₂O₃/MgAl-h, respectively. These
187 weight reductions were attributed to two processes: the decomposition of interlamellar carbonate
188 and the dehydroxylation of the hydrotalcite sheets (Ramos-Ramírez *et al.*, 2019). In this
189 temperature range, the lamellar structure underwent distortion due to the formation of mixed oxides
190 (Rey *et al.*, 1992). This distortion led to the emergence of exothermic peaks at approximately 350
191 and 550 °C, corresponding to the dehydroxylation of the brucite-like layers and the decomposition
192 of incorporated anions, as explained by (Wang *et al.*, 2007).

193

194

195

196

197

198

199

200

201

202

203

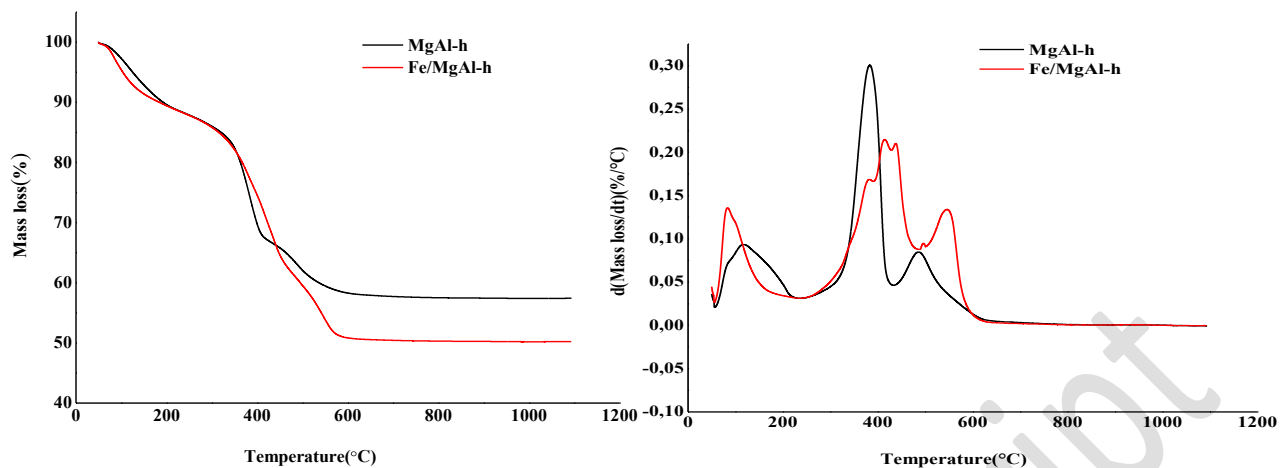
204

Fig.1. ATG/DTG of non-calcined MgAl-h and Fe/MgAl-h

204

205 The infrared spectra presented in Figure 2 for our samples exhibit typical characteristics associated
 206 with lamellar double hydroxides, consistent with findings from previous studies on hydrotalcites
 207 (Fernández *et al.*, 1998; Das *et al.*, 2002b; Ferreira *et al.*, 2004). To know that the spectral
 208 characteristics of Fe/MgAl closely match those documented in prior literature, as evidenced by the
 209 findings of (Riman *et al.*, 2002; Chebout *et al.*, 2010; Mamat *et al.*, 2014; Kerchiche *et al.*,
 210 2017). These spectra reveal similar vibration bands. Specifically, a broad band observed between
 211 3450 - 3500 cm^{-1} is attributed to the presence of hydroxide groups (OH) within the layers and to
 212 intercalated and/or adsorbed water molecules. Another vibration band in the range of 1630-1640
 213 cm^{-1} can be ascribed to the deformation of intercalated water molecules HOH (δHOH) (Leofanti *et*
 214 *al.*, 1998).

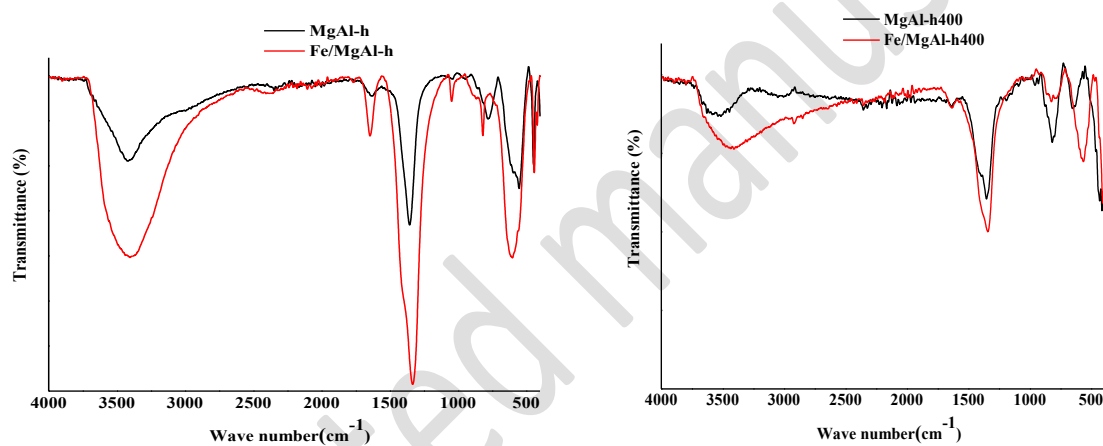
215 The main bands associated with intercalated and adsorbed anions are observed within the 2000 to
 216 1000 cm^{-1} range (Cavani *et al.*, 1991). Furthermore, the remaining bands below 1000 cm^{-1}
 217 correspond to vibrations of M–O–M, which are characteristic of the double lamellar structure (Das
 218 *et al.*, 2002b). Notably, a persistent vibration at 1450 cm^{-1} , observed in the material Fe/MgAl-h400,



219 is indicative of the presence of maghemite iron oxide ($\gamma\text{-Fe}_2\text{O}_3$). In Figure 2, it is evident that the
220 peak intensities related to water dehydration and dehydroxylation decrease, a phenomenon
221 attributed to the calcination of the materials at 400 °C(Barakat, 2012; Kerchich *et al.*, 2021).

222

223 the elemental analyses of the samples are reported in Table.1, shown that the experimental molar
224 ratios $\text{M}^{2+}/\text{M}^{3+}$ are in good agreement with the theoretical values ($\text{M}^{2+}/\text{M}^{3+} = 2$). On the other hand,
225 $\text{M}^{3+}/(\text{M}^{2+} + \text{M}^{3+})$ values are between 0.31 and 0.32, these values correspond to the optimal ratios
226 necessary for achieving a well-formed crystalline LDH structure (Miyata, 1983; Fernández *et al.*,
227 1998; Leofanti *et al.*, 1998; Das *et al.*, 2002a; Barakat, 2012; Mamat *et al.*, 2014).



228

229 **Fig.2.** FTIR spectra of the not calcined MgAl-h and calcined Fe/MgAl-h400

230

231

232

233

234

235 **Table.1** Chemical analysis and band gap energies of MgAl-h, Fe/MgAl-h and Fe/MgAl-c materials
236 calcined at 400C°

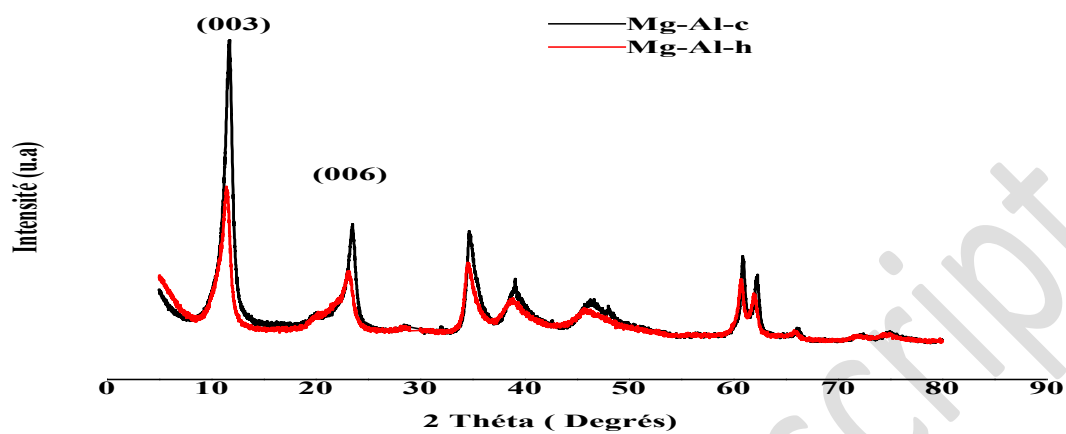
Samples	T °C	Formulas	M^{2+}/M^{3+}		$x =$	%	Eg
			$(M^{2+}/M^{3+})_{theo}$	$(M^{2+}/M^{3+})_{ex}$	$M^{3+}/(M^{2++}$	Fe	(eV)
				p	$M^{3+})$		
MgAl-h	400	$Mg_{0.68}Al_{0.32}$ -h	2	2.1	0.32	-	-
Fe₂O₃/MgAl-h	400	$Fe/Mg_{0.69}Al_{0.31}$ -h	2	2.22	0.31	7.73	1.89
Fe₂O₃/MgAl-c	400	$Fe/Mg_{0.68}Al_{0.32}$ -c	2	2.06	0.32	9.73	2.02

237

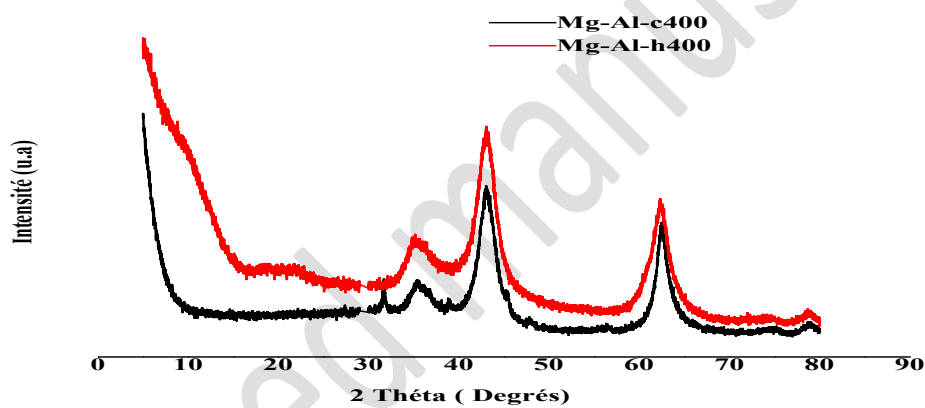
238 The X-ray diffraction (XRD) patterns presented in Figure 3 offer valuable insights into the samples
239 we prepared. These patterns exhibit distinctive characteristics for various samples, such as non-
240 calcined samples Mg-Al-h and Mg-Al-c, as well as calcined samples such as Mg-Al-h400, Mg-Al-
241 c400, Fe/Mg-Al-h400, and Fe/Mg-Al-c400. Notably, these patterns reveal prominent diffraction
242 peaks at specific 2θ values (11.87, 23.75, 34.76, 39.1, 46.49, 61.12, 62.26, 66.32, 72.48, and 75.08°)
243 corresponding to the (003), (006), (009), (012), (018), (110), and (113) planes. These peaks
244 unequivocally confirm the presence of the MgAl structure, consistent with data from PDF-#38-
245 0487, which describes a rhombohedral structure (Chen & Qu, 2003; Lakraimi *et al.*, 2006; Hong *et*
246 *al.*, 2014). However, it's important to note that the absence of peaks corresponding to (003) and
247 (006) after heat treatment indicates the disintegration of the hydrotalcites lamellar structure,
248 aligning with previous research findings (Chebout *et al.*, 2010; Kerchiche *et al.*, 2017; Ramos-
249 Ramírez *et al.*, 2020). This transformation suggests a shift from the hydrotalcite structure to oxides.
250 Remarkably, new peaks emerge at 2θ values of 31.74, 35.35, 42.91, 62.40, 74.89, and 78.60°,
251 indicating the presence of MgO (JCPDS No. 87-0653). In contrast, for Fe/MgAl, diffraction peaks
252 appear at 2θ values of 22.9, 29.1, 31.6, 39.0, 48.3, 55.6, and 56.6°, clearly indicating the presence of
253 iron oxide in the γ -phase (γ -Fe₂O₃, maghemite). The corresponding interlayer spacing (d₀₀₃),
254 approximately 0.8 nm for all three samples, is consistent with a Mg/Al molar ratio close to 2 in the
255 brucite-like layers and the presence of carbonate as charge compensating anions, as reported in

256 previous studies (Wang *et al.*, 2007; Chebout *et al.*, 2010; Kerchiche *et al.*, 2017).

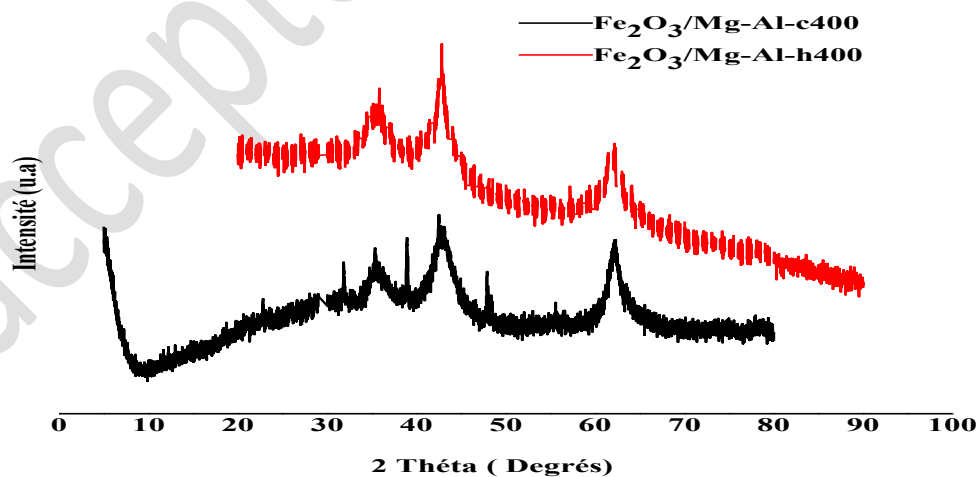
257



258



259



260

261 **Fig.3.** XRD patterns of (a) MgAl-h, MgAL-c, (b) MgAl-h400, MgAl-c400 and (c) Fe/MgAl-h400,

262

Fe/MgAl-c400

263

264 The "a" parameter, representing the average metal-to-metal distance within the layers and
265 determined from the (110) diffraction line, was found to be 0.3 nm for the MgAl sample and 0.2 nm
266 for the Fe/MgAl sample. This observation substantiates the alteration in the composition of
267 hydrotalcite layers in the presence of Fe³⁺. These computed values align closely with those
268 documented in previous studies (Millange *et al.*, 2000; Chebout *et al.*, 2010; León *et al.*, 2010;
269 Kerchiche *et al.*, 2017).

270 The size of crystallite particles (D) was calculated using the Debye-Scherrer equation (Tichit *et al.*,
271 2006). For MgAl-h400, Fe/MgAl-h400, and Fe/MgAl-c400, the calculated D values are
272 approximately 2.1 nm, 3.8 nm, and 3.5 nm, respectively. These results indicate an increase in
273 particle size due to the presence of iron content, as demonstrated in the work by (Kerchich *et al.*,
274 2021). Furthermore, it is worth noting that the hydrothermal preparation method for Mg-Al
275 confirmed an enhancement in crystallinity.

276 The SEM micrograph in Figure 4a reveals that the hydrothermal method yielded a synthetic MgAl-
277 h material exhibiting a plate-like structure characteristic of lamellar phases. Upon calcination, as
278 depicted in the micrographs in Figure 4b and c, it becomes evident that the material exhibits
279 enhanced crystallinity and an increase in particle size when compared to the hydrothermal method.
280 Additionally, the surface of the hydrotalcite is conspicuously adorned with uniformly dispersed iron
281 oxide nanoparticles, creating a relatively homogeneous appearance of γ -Fe₂O₃ (Barakat, 2012;
282 Kerchich *et al.*, 2021).

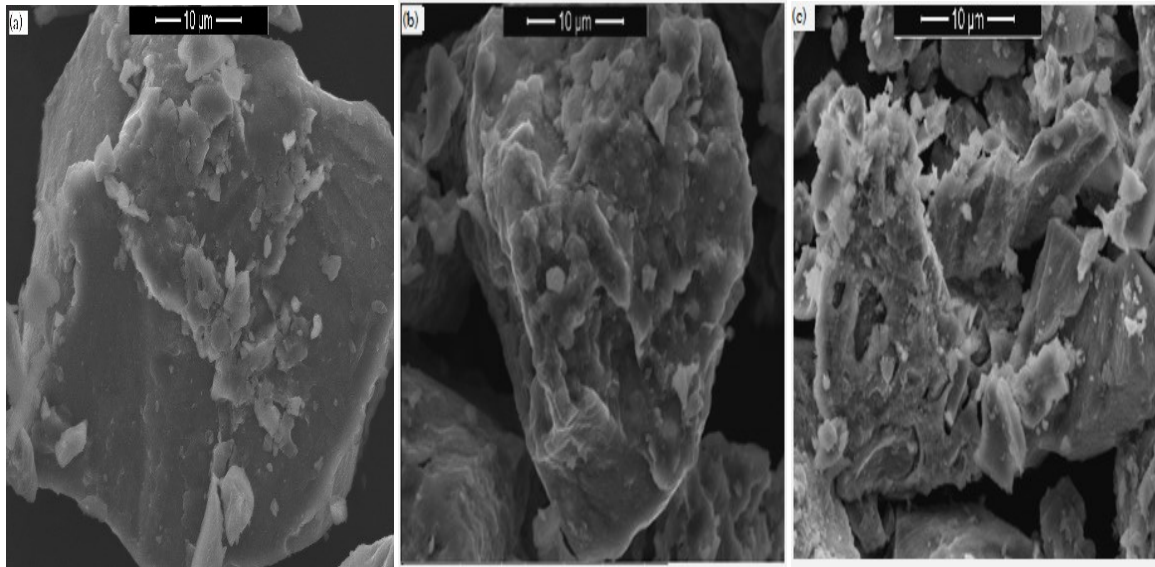


Fig.4. SEM images: (a) MgAl-h, (b) Fe/MgAl-h400 and (c) Fe/MgAl-c400

283

284

285

286 Hence, an increase in the cristallinty signifies a reduction in the bandgap width, a concept supported
 287 by various studies (Burstein, 1954; Moss, 1954; Aliahmad & Nasiri Moghaddam, 2013). This
 288 relationship is corroborated by our assessment of the bandgap (E_g) in our samples using Tauc's
 289 equation (Tauc *et al.*, 1966), expressed as:

290

$$(\alpha h\nu)^m = B (h\nu - E_g) \quad (1)$$

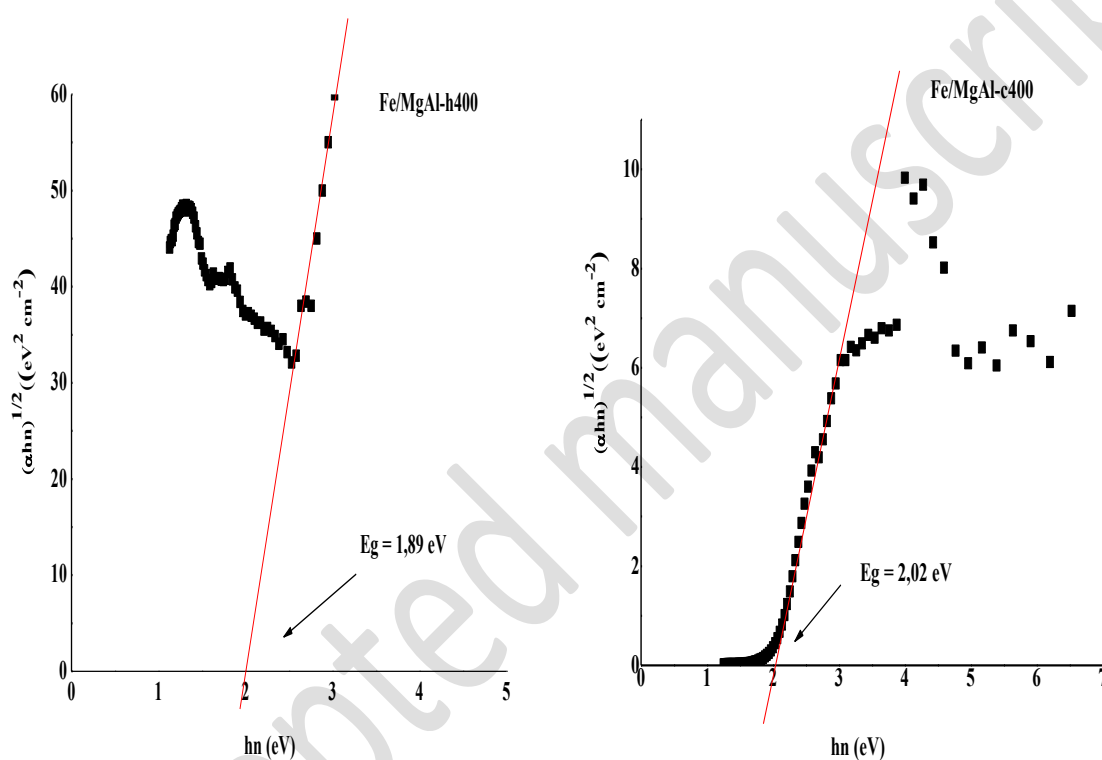
291 In this equation, B represents a constant, E_g denotes the optical gap energy, α stands for the optical
 292 absorption coefficient, $h\nu$ represents the energy of the photon, h is the Planck constant, and ν
 293 signifies photon frequency. The value of E_g is determined by plotting $(\alpha h\nu)^m$ against $(h\nu)$ and
 294 extrapolating the linear portion of the curve that intersects the energy axis $h\nu$. For direct gap
 295 materials, this corresponds to $m = 2$, whereas for indirect gap materials, it's $m = 1/2$.

296 Fe/MgAl-h400 exhibited an indirect band gap energy with a value of 1.89 eV, compared to
 297 Fe/MgAl-c400 exhibited a direct band gap energy with a values of 2.02 (Fig. 5). Thus, the band gap
 298 values of synthesis materials are slightly lower than that of the bulk Fe_2O_3 (2.1 eV). This widening
 299 of the prohibited band is an effect of the quantum confinement observed in many other synthesized
 300 semiconductor materials (Wen *et al.*, 2005; Bepari *et al.*, 2017). So, such narrow band gap is

301 beneficial for the efficient utilization of visible light (Iron oxide exhibits a red color, which can
302 absorb in the visible region). The narrower band gap of the material can harvest more photons to
303 excite the e⁻ from the valence band (VB) to the conduction band (CB) and thus, the photocatalytic
304 activity is increased.

305

306



307

308 **Fig.5.** Band gap energies of calcined Fe/MgAl-h400 and Fe/MgAl-c400

309

310 **Gap type effect on photocatalytic degradation by Fe/MgAl- photocatalyst**

311 The photocatalytic activity of the synthesized Fe/MgAl-h400 material was evaluated for the
312 degradation of MB dye in aqueous solution. The tests examined with the hydrothermal method
313 under artificial irradiation using a tungsten lamp as visible light, under the same conditions which
314 are applied for the evolution of the catalytic activity of the Fe/MgAl-c400 material prepared by the

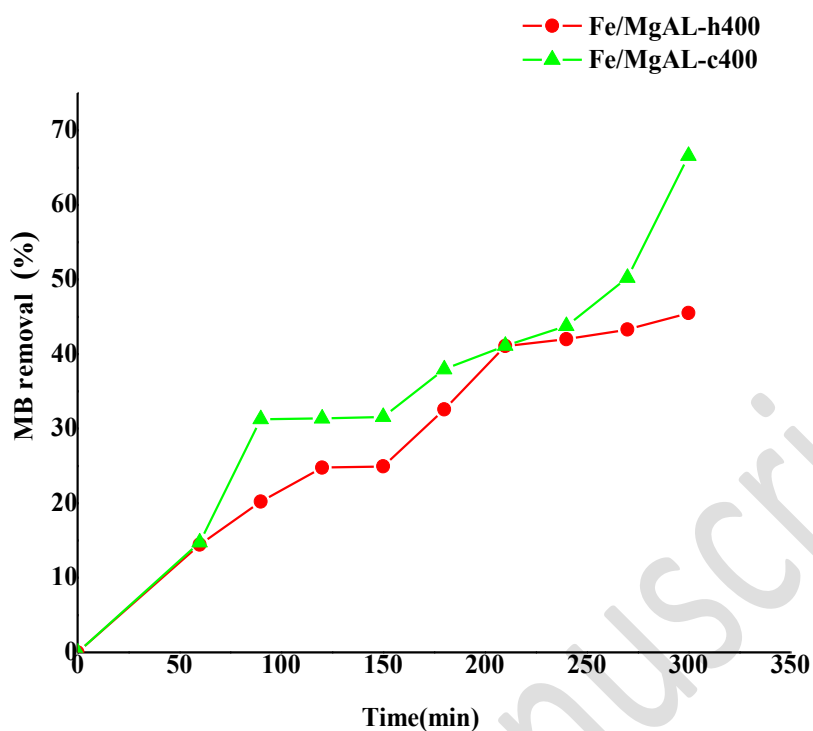
315 coprecipitation method. Namely, the mass percentage of iron, the dye concentration, the amount of
316 photocatalyst, the temperature of calcinations and at a free pH (5.9). Using MB concentration of 50
317 mg/L and a catalyst amount of 0,5 g/L, it is can be easily observed that MB removal increased
318 efficiency with the reaction time (Fig.6). The yield obtained from the degradation of MB is as
319 expected due to the presence of iron oxide with a maghemite structure ($\gamma\text{-Fe}_2\text{O}_3$)(Kerchich *et al.*,
320 2021), that is a semiconductor generally known for its visible band gap energy (~ 2.1 eV). So, the
321 supported catalysts on an inert support as hydrotalcite structure increase the metal dispersion, and
322 the photo-activity depended particularly on the particle (Boudjemaa *et al.*, 2009; Boudjemaa &
323 Trari, 2010). According to the data shown in Fig. 6, the highest reactivity is observed with with the
324 photocatalyst prepared by the Fe/MgAl-c400 coprecipitation. After 240 min of irradiation the
325 reaction efficiency is around of 67 and 46% for Fe/MgAl-c400 and Fe/MgAl-h400 photocatalysts,
326 respectively.

327 To compare the performance of two synthesis methods, hydrothermal and coprecipitation, in the
328 context of photodegradation, the results clearly indicate that MgAl-h400 exhibits lower
329 photodegradation. Despite their impressive fundamental properties as adsorbents, lamellar
330 structures are less frequently employed in photocatalytic reactions(Figueras, 2004; Figueras *et al.*,
331 2006) . Photocatalysis operates on the principle of degrading materials under the influence of light
332 with energy equal to or greater than its band gap ($h\nu \geq E_g$). This process involves catalyzing
333 chemical reactions through electronically excited species generated by photon absorption
334 (Khatamian *et al.*, 2010; Dessie, 2017; Terna *et al.*, 2021).

335 When the material is irradiated with a photon with energy greater than or equal to the band gap
336 (E_g), it results in the generation of an electron-hole pair (e^-/h^+), leading to the formation of hydroxyl
337 radicals (OH^\bullet) and superoxide anion radicals ($\text{O}_2^{\bullet-}$), as well as the photogenerated hole (h^+)
338 responsible for the degradation of organic molecules. Under irradiation, the h^+ hole reacts with
339 water to produce OH^\bullet radicals. It has been previously demonstrated by (Kerchich *et al.*, 2021), that

340 OH[•] radicals and h⁺ holes are the reactive species involved in the photodegradation of MB
341 (methylene blue) for Fe/MgAl-400 materials. A photocatalysis goes beyond the adsorption property
342 of solids (adsorbents) to capture certain adsorbates on their surfaces, therefore does not is not just
343 based on the property that solids have of fixing certain adsorbates on their surface. Hence, based on
344 the gap results, we can conclude that the main difference in lies in the direct and indirect band gaps
345 exhibited by the Fe/MgAl-c400 and Fe/MgAl-h400 semiconductors, respectively.

346 The fundamental distinction between direct and indirect band gaps lies in their crystal momentum
347 characteristics. In a direct band gap semiconductor, both electrons and holes possess identical
348 crystal momentum values in the conduction and valence bands, enabling direct photon emission by
349 an electron. Conversely, indirect band gap semiconductors lack this symmetry, making it
350 impossible for an electron to directly emit a photon since photons cannot carry crystal momentum.
351 For radiative recombination to take place in an indirect band gap material, it necessitates the
352 involvement of phonon absorption or emission, where the phonon's momentum compensates for the
353 difference between the electron and hole momenta. However, this process occurs at a considerably
354 slower pace because it relies on the intersection of three entities: an electron, a photon, and a
355 phonon. As a result, the recombination process is significantly more efficient in direct band gap
356 semiconductors compared to indirect band gap semiconductors. In the case of indirect band gap
357 semiconductors, the recombination process relies on phonon mediation, which results in a lower
358 photocatalytic efficiency compared to direct band gap semiconductors (Johari & Shenoy, 2012;
359 Conley *et al.*, 2013; Gabal *et al.*, 2023). In conclusion, a wider band gap increases the density of
360 electronic states in the material. This means that there are more sites available for chemical
361 reactions, which can facilitate the degradation of dyes. Excited electrons from the valence band can
362 more easily interact with other molecules and chemically react to degrade the dyes.



363

364 **Fig.6.** Effect of the synthesis method on the removal of MB (50ppm BM, 0.5g/l mass photocatalys,
 365 free pH (5,9))

366

367 **Conclusion**

368 The research presented in this article contributes to the advancement of knowledge by focusing on
 369 the development of novel photocatalysts based on iron oxide within the lamellar double hydroxide
 370 structure, and their application in environmental contexts. Hydrotalcite-based materials have
 371 garnered significant interest in recent decades due to their simple synthesis processes and wide
 372 range of applications. These materials are predominantly synthesized through co-precipitation and
 373 hydrothermal methods, enabling the combination of M(II) and M(III) cations along with interlayer
 374 anions within the hydrotalcite structure. The unique structural properties of hydrotalcite make it a
 375 promising candidate for various applications, particularly in the field of photocatalysis.

376 This study successfully demonstrated the effectiveness of the hydrothermal method in synthesizing
 377 a new photocatalyst, Fe/MgAl-h400, based on iron. The key findings of the research are as follows:

- 378 - The Fe/MgAl-h400 photocatalyst was synthesized using the impregnation method and
379 underwent comprehensive physico-chemical characterization, including XRF, XRD, SEM,
380 ATG/DSC, RDs, and FTIR techniques.
- 381 - The infrared spectra exhibited typical characteristics associated with lamellar double
382 hydroxides, consistent with previous studies on hydrotalcites, and the XRD results clearly
383 indicated the presence of iron oxide.
- 384 - The Fe/MgAl-h400 photocatalyst demonstrated improved crystallinity and remarkable
385 photoactivity under visible light. After 240 minutes of irradiation, the Fe/MgAl-h400
386 photocatalyst, with a particle size of approximately 3.8 nm and an indirect bandgap energy
387 of 1.89 eV, exhibited a notable photodegradation rate of approximately 46%.
- 388 - The Fe/MgAl-h400 semiconductor, with an indirect bandgap, undergoes a recombination
389 process that depends on phonon mediation, leading to lower photocatalytic efficiency
390 compared to direct bandgap semiconductors. However, a wider bandgap in semiconductor
391 materials provides notable advantages for dye degradation, including enhanced light
392 absorption, increased reactivity with dyes, greater stability, and improved durability.
- 393 - Therefore, enhancing the qualities and modifying the basic properties of mixed oxides
394 derived from hydrotalcite precursors is highly beneficial. These modifications facilitate
395 reactions that require varying basic strength and contribute to more efficient and controlled
396 degradation of dyes, which is crucial in fields such as wastewater treatment, air purification,
397 and the removal of unwanted dyes.

398 **References**

- 399 Aliahmad, M. & Nasiri Moghaddam, N. (2013) Synthesis of maghemite (γ -Fe₂O₃) nanoparticles by
400 thermal-decomposition of magnetite (Fe₃O₄) nanoparticles. *Materials Science-Poland*, **31**,
401 264–268.

402 ALLMANN, R. & HP, J. (1969) *DIE STRUKTUR DES HYDROTALKITS.*, Neues Jahrb Mineral
403 Monatsh.

404 Allou, N.B., Saikia, P., Borah, A. & Goswamee, R.L. (2017) Hybrid nanocomposites of layered
405 double hydroxides: an update of their biological applications and future prospects. *Colloid
406 and Polymer Science*, **295**, 725–747.

407 Ameena Shirin, V.K., Sankar, R., Johnson, A.P., Gangadharappa, H.V. & Pramod, K. (2021)
408 Advanced drug delivery applications of layered double hydroxide. *Journal of Controlled
409 Release*, **330**, 398–426.

410 Arrabito, G., Bonasera, A., Prestopino, G., Orsini, A., Mattoccia, A., Martinelli, E., Pignataro, B. &
411 Medaglia, P.G. (2019) Layered Double Hydroxides: A Toolbox for Chemistry and Biology.
412 *Crystals*, **9**, 361.

413 Asif, M., Haitao, W., Shuang, D., Aziz, A., Zhang, G., Xiao, F. & Liu, H. (2017) Metal oxide
414 intercalated layered double hydroxide nanosphere: With enhanced electrocatalytic activity
415 towards H₂O₂ for biological applications. *Sensors and Actuators B: Chemical*, **239**, 243–
416 252.

417 Barakat, N.A.M. (2012) Synthesis and characterization of maghemite iron oxide (γ -Fe₂O₃)
418 nanofibers: novel semiconductor with magnetic feature. *Journal of Materials Science*, **47**,
419 6237–6245.

420 Bepari, R.A., Bharali, P. & Das, B.K. (2017) Controlled synthesis of α - and γ -Fe₂O₃ nanoparticles
421 via thermolysis of PVA gels and studies on α -Fe₂O₃ catalyzed styrene epoxidation. *Journal
422 of Saudi Chemical Society*, **S1**, S170–S178.

423 Boudjemaa, A., Boumaza, S., Trari, M., Bouarab, R. & Bouguelia, A. (2009) Physical and photo-
424 electrochemical characterizations of α -Fe₂O₃. Application for hydrogen production.
425 *International Journal of Hydrogen Energy*, **34**, 4268–4274.

- 426 Boudjemaa, A. & Trari, M. (2010) Photo-catalytic hydrogen production over Fe₂O₃ based
427 catalysts. *International Journal of Hydrogen Energy*, **35**, 7684–7689.
- 428 Burstein, E. (1954) Anomalous Optical Absorption Limit in InSb. *Physical Review*, **93**, 632–633.
- 429 Carja, G., Chitanu, G.C., Kameshima, Y., Chiriac, H. & Okada, K. (2008) LDH–maleic anhydride
430 copolymers as new hybrid materials and their textural organisation. *Applied Clay Science*,
431 **41**, 107–112.
- 432 Cavalcanti, F.A.P., Schutz, A. & Biloen, P. (1987) *Interlayer Accessibility in Layered Double-*
433 *Metal Hydroxides. Studies in Surface Science and Catalysis Preparation of Catalysts IV.* (ed.
434 by B. Delmon), P. Grange), P.A. Jacobs), and G. Poncelet), pp. 165–174. Elsevier.
- 435 Cavani, F., Trifirò, F. & Vaccari, A. (1991) Hydrotalcite-type anionic clays: Preparation, properties
436 and applications. *Catalysis Today*, **11**, 173–301.
- 437 Chebout, R., Tichit, D., Layrac, G., Barama, A., Coq, B., Cota, I., Rangel, E.R. & Medina, F.
438 (2010) New basic catalysts obtained from layered double hydroxides nanocomposites. *Solid*
439 *State Sciences*, **12**, 1013–1017.
- 440 Chen, M., Hou, C., Huo, D., Fa, H., Zhao, Y. & Shen, C. (2017) A sensitive electrochemical DNA
441 biosensor based on three-dimensional nitrogen-doped graphene and Fe₃O₄ nanoparticles.
442 *Sensors and Actuators B: Chemical*, **239**, 421–429.
- 443 Chen, W. & Qu, B. (2003) Structural Characteristics and Thermal Properties of PE-g-MA/MgAl-
444 LDH Exfoliation Nanocomposites Synthesized by Solution Intercalation. *Chemistry of*
445 *Materials*, **15**, 3208–3213.
- 446 Choudary, B.M., Madhi, S., Chowdari, N.S., Kantam, M.L. & Sreedhar, B. (2002) Layered Double
447 Hydroxide Supported Nanopalladium Catalyst for Heck-, Suzuki-, Sonogashira-, and Stille-
448 Type Coupling Reactions of Chloroarenes. *Journal of the American Chemical Society*, **124**,
449 14127–14136.

- 450 Conley, H.J., Wang, B., Ziegler, J.I., Haglund, R.F., Pantelides, S.T. & Bolotin, K.I. (2013)
451 Bandgap engineering of strained monolayer and bilayer MoS₂. *Nano Letters*, **13**, 3626–
452 3630.
- 453 Crepaldi, E.L., Pavan, P.C. & Valim, J.B. (2000) Anion exchange in layered double hydroxides by
454 surfactant salt formation. *Journal of Materials Chemistry*, **10**, 1337–1343.
- 455 Das, J., Das, D., Dash, G.P. & Parida, K.M. (2002a) Studies on Mg/Fe hydrotalcite-like-compound
456 (HTlc) I. Removal of inorganic selenite (SeO₃(2-)) from aqueous medium. *Journal of*
457 *Colloid and Interface Science*, **251**, 26–32.
- 458 Das, J., Das, D., Dash, G.P. & Parida, K.M. (2002b) Studies on Mg/Fe Hydrotalcite-Like-
459 Compound (HTlc): I. Removal of Inorganic Selenite (SeO₃²⁻) from Aqueous Medium.
460 *Journal of Colloid and Interface Science*, **251**, 26–32.
- 461 Desportes, S., Steinmetz, D., Hémati, M., Philippot, K. & Chaudret, B. (2005) Production of
462 supported asymmetric catalysts in a fluidised bed. *Powder Technology*, **157**, 12–19.
- 463 Dessie, Y. (2017) Optical Photocatalytic Degradation of Methylene Blue Using Lignocellulose
464 Modified TiO₂. *American Journal of Optics and Photonics*, **5**, 55.
- 465 Fan, G., Li, F., Evans, D.G. & Duan, X. (2014) Catalytic applications of layered double hydroxides:
466 recent advances and perspectives. *Chemical Society Reviews*, **43**, 7040–7066.
- 467 Faour, A., Prévot, V. & Taviot-Gueho, C. (2010) Microstructural study of different LDH
468 morphologies obtained via different synthesis routes. *Journal of Physics and Chemistry of*
469 *Solids*, **71**, 487–490.
- 470 Fernández, J.M., Ulibarri, M.A., Labajos, F.M. & Rives, V. (1998) The effect of iron on the
471 crystalline phases formed upon thermal decomposition of Mg-Al-Fe hydrotalcites. *Journal*
472 *of Materials Chemistry*, **8**, 2507–2514.

- 473 Ferreira, O.P., Alves, O.L., Gouveia, D.X., Souza Filho, A.G., de Paiva, J.A.C. & Filho, J.M.
474 (2004) Thermal decomposition and structural reconstruction effect on Mg–Fe-based
475 hydrotalcite compounds. *Journal of Solid State Chemistry*, **177**, 3058–3069.
- 476 Figueras, F. (2004) Base Catalysis in the Synthesis of Fine Chemicals. *Topics in Catalysis*, **29**, 189–
477 196.
- 478 Figueras, F., Kantam, M.L. & Choudary, B.M. (2006) Solid Base Catalysts in Organic Synthesis.
479 *Current Organic Chemistry*, **10**, 1627–1637.
- 480 Gabal, M.A., Al-Harthy, E.A., Al Angari, Y.M., Awad, A., Al-Juaid, A.A. & Saeed, A. (2023)
481 Synthesis, characterization and electrical properties of polypyrrole/Mn_{0.8}Zn_{0.2}Fe₂O₄/GO
482 ternary hybrid composites using spent Zn-C batteries. *Journal of Sol-Gel Science and*
483 *Technology*, **105**, 781–792.
- 484 Garcia-Gallastegui, A., Iruretagoyena, D., Gouvea, V., Mokhtar, M., Asiri, A.M., Basahel, S.N., Al-
485 Thabaiti, S.A., Alyoubi, A.O., Chadwick, D. & Shaffer, M.S.P. (2012) Graphene Oxide as
486 Support for Layered Double Hydroxides: Enhancing the CO₂ Adsorption Capacity.
487 *Chemistry of Materials*, **24**, 4531–4539.
- 488 Hong, J., Zhang, W., Wang, Y., Zhou, T. & Xu, R. (2014) Photocatalytic Reduction of Carbon
489 Dioxide over Self-Assembled Carbon Nitride and Layered Double Hydroxide: The Role of
490 Carbon Dioxide Enrichment. *ChemCatChem*, **6**, 2315–2321.
- 491 Islam, D.A., Barman, K., Jasimuddin, S. & Acharya, H. (2019) Synthesis of ultrasmall and
492 monodisperse sulfur nanoparticle intercalated CoAl layered double hydroxide and its
493 electro-catalytic water oxidation reaction at neutral pH. *Nanoscale*, **11**, 7560–7566.
- 494 Islam, D.A., Borah, D. & Acharya, H. (2015) Controlled synthesis of monodisperse silver
495 nanoparticles supported layered double hydroxide catalyst. *RSC Advances*, **5**, 13239–13245.

- 496 Jing, F., Zhang, Y., Luo, S., Chu, W. & Qian, W. (2010) Nano-size MZnAl (M=Cu, Co, Ni) metal
497 oxides obtained by combining hydrothermal synthesis with urea homogeneous precipitation
498 procedures. *Applied Clay Science*, **48**, 203–207.
- 499 Johari, P. & Shenoy, V.B. (2012) Tuning the Electronic Properties of Semiconducting Transition
500 Metal Dichalcogenides by Applying Mechanical Strains. *ACS Nano*, **6**, 5449–5456.
- 501 Kerchich, S., Boudjemaa, A., Chebout, R., Bachari, K. & Mameri, N. (2021) High performance of
502 δ -Fe₂O₃ novel photo-catalyst supported on LDH structure. *Journal of Photochemistry and*
503 *Photobiology A: Chemistry*, **406**, 113001.
- 504 Kerchiche, S., Chebout, R., Barama, A. & Bachari, K. (2017) New way for iron introduction in
505 LDH matrix used as catalysts for Friedel–Crafts reactions. *Arabian Journal of Chemistry*,
506 **10**, S328–S333.
- 507 Khatamian, M., Daneshvar, N. & Sabaee, S. (2010) Heterogeneous Photocatalytic Decolorization of
508 Brown NG by TiO₂ –UV Process. *Iranian Journal of Chemistry and Chemical Engineering*,
509 **29**, 19–26.
- 510 Klemkaite, K., Prosycevas, I., Taraskevicius, R., Khinsky, A. & Kareiva, A. (2011) Synthesis and
511 characterization of layered double hydroxides with different cations (Mg, Co, Ni, Al),
512 decomposition and reformation of mixed metal oxides to layered structures. *Open*
513 *Chemistry*, **9**, 275–282.
- 514 Klopogge, J.T., Hickey, L. & Frost, R.L. (2004) The effects of synthesis pH and hydrothermal
515 treatment on the formation of zinc aluminum hydroxalicates. *Journal of Solid State*
516 *Chemistry*, **177**, 4047–4057.
- 517 Lakraimi, M., Legrouri, A., Barroug, A., De Roy, A. & Besse, J.P. (2006) Synthesis and
518 characterisation of a new stable organo-mineral hybrid nanomaterial: 4-
519 Chlorobenzenesulfonate in the zinc–aluminium layered double hydroxide. *Materials*
520 *Research Bulletin*, **41**, 1763–1774.

- 521 Leofanti, G., Padovan, M., Tozzola, G. & Venturelli, B. (1998) Surface area and pore texture of
522 catalysts. *Catalysis Today*, **41**, 207–219.
- 523 León, M., Díaz, E., Bennici, S., Vega, A., Ordóñez, S. & Auroux, A. (2010) Adsorption of CO₂ on
524 Hydrotalcite-Derived Mixed Oxides: Sorption Mechanisms and Consequences for
525 Adsorption Irreversibility. *Industrial & Engineering Chemistry Research*, **49**, 3663–3671.
- 526 Mamat, M., Tagg, T., Khairul, W.M., Abdullah, M.A.A., Tahir, N.M., Jubri, Z. & As'ari, R.A.
527 (2014) Behavior of Layered Double Hydroxides Having Different Divalent Transition Metal
528 Groups. *Applied Mechanics and Materials*, **563**, 94–101.
- 529 Millange, F., Walton, R.I. & O'Hare, D. (2000) Time-resolved in situ X-ray diffraction study of the
530 liquid-phase reconstruction of Mg–Al–carbonate hydrotalcite-like compounds. *Journal of*
531 *Materials Chemistry*, **10**, 1713–1720.
- 532 Mishra, G., Dash, B. & Pandey, S. (2018a) Layered double hydroxides: A brief review from
533 fundamentals to application as evolving biomaterials. *Applied Clay Science*, **153**, 172–186.
- 534 Mishra, G., Dash, B., Pandey, S. & Sethi, D. (2018b) Ternary layered double hydroxides (LDH)
535 based on Cu- substituted ZnAl for the design of efficient antibacterial ceramics. *Applied*
536 *Clay Science*, **165**, 214–222.
- 537 Miyata, S. (1983) Anion-Exchange Properties of Hydrotalcite-Like Compounds. *Clays and Clay*
538 *Minerals*, **31**, 305–311.
- 539 Miyata, S. (1980) Physico-Chemical Properties of Synthetic Hydrotalcites in Relation to
540 Composition. *Clays and Clay Minerals*, **28**, 50–56.
- 541 Miyata, S. & Kumura, T. (1973) Synthesis of new hydrotalcite-like compounds and their physico-
542 chemical properties. *Chemistry Letters*, **2**, 843–848.
- 543 Moss, T.S. (1954) The Interpretation of the Properties of Indium Antimonide. *Proceedings of the*
544 *Physical Society. Section B*, **67**, 775.

- 545 Nishio, K., Ikeda, M., Gokon, N., Tsubouchi, S., Narimatsu, H., Mochizuki, Y., Sakamoto, S.,
546 Sandhu, A., Abe, M. & Handa, H. (2007) Preparation of size-controlled (30–100nm)
547 magnetite nanoparticles for biomedical applications. *Journal of Magnetism and Magnetic*
548 *Materials*, **310**, 2408–2410.
- 549 Oliveira, L.C.A., Rios, R.V.R.A., Fabris, J.D., Sapag, K., Garg, V.K. & Lago, R.M. (2003) Clay–
550 iron oxide magnetic composites for the adsorption of contaminants in water. *Applied Clay*
551 *Science*, **22**, 169–177.
- 552 Patel, R., Park, J.T., Patel, M., Dash, J.K., Gowd, E.B., Karpoormath, R., Mishra, A., Kwak, J. &
553 Kim, J.H. (2017) Transition-metal-based layered double hydroxides tailored for energy
554 conversion and storage. *Journal of Materials Chemistry A*, **6**, 12–29.
- 555 Peng, F., Luo, T. & Yuan, Y. (2014) Controllable synthesis of Mg–Fe layered double hydroxide
556 nanoplates with specific Mg/Fe ratios and their effect on adsorption of As(V) from water.
557 *New Journal of Chemistry*, **38**, 4427–4433.
- 558 Pengfei, Y., Yuanxin, X., Na, Y. & Yong, A. (2020) Preparation of Uniform Highly Dispersed Mg–
559 Al-LDHs and Their Adsorption Performance for Chloride Ions. *Industrial & Engineering*
560 *Chemistry Research*, **59**, 10697–10704.
- 561 Qin, Y., Zhao, R. & Bai, C. (2020) Layered double hydroxide-oriented assembly by negatively
562 charged graphene oxide for NO₂ sensing at ppb level. *New Journal of Chemistry*, **44**,
563 16985–16994.
- 564 Ramos-Ramírez, E., Gutiérrez-Ortega, N.L., Tzompantzi-Morales, F., Barrera-Rodríguez, A.,
565 Castillo-Rodríguez, J.C., Tzompantzi-Flores, C., Santolalla-Vargas, C.E. & Guevara-
566 Hornedo, M. del P. (2020) Photocatalytic Degradation of 2,4-Dichlorophenol on NiAl-
567 Mixed Oxides Derivatives of Activated Layered Double Hydroxides. *Topics in Catalysis*,
568 **63**, 546–563.

569 Ramos-Ramírez, E., Tzompantzi-Morales, F., Gutiérrez-Ortega, N., Mojica-Calvillo, H.G. &
570 Castillo-Rodríguez, J. (2019) Photocatalytic Degradation of 2,4,6-Trichlorophenol by MgO–
571 MgFe₂O₄ Derived from Layered Double Hydroxide Structures. *Catalysts*, **9**, 454.

572 Reichle, W.T. (1985) Catalytic reactions by thermally activated, synthetic, anionic clay minerals.
573 *Journal of Catalysis*, **94**, 547–557.

574 Reichle, W.T. (1986) Synthesis of anionic clay minerals (mixed metal hydroxides, hydrotalcite).
575 *Solid State Ionics*, **22**, 135–141.

576 Rey, F., Fornés, V. & Rojo, J.M. (1992) Thermal decomposition of hydrotalcites. An infrared and
577 nuclear magnetic resonance spectroscopic study. *Journal of the Chemical Society, Faraday*
578 *Transactions*, **88**, 2233–2238.

579 Riman, R.E., Suchanek, W.L. & Lencka, M.M. (2002) Hydrothermal crystallization of ceramics.
580 *Annales de Chimie Science des Matériaux*, **27**, 15–36.

581 Sels, B.F., De Vos, D.E. & Jacobs, P.A. (2001) Hydrotalcite-like anionic clays in catalytic organic
582 reactions. *Catalysis Reviews*, **43**, 443–488.

583 da Silva, D.C., Neto, K.S., Coaquira, J.A.H., Araujo, P.P., Cintra, D.O.S., Lima, E.C.D., Guilherme,
584 L.R., Mosiniewicz-Szablewska, E. & Morais, P.C. (2010) Magnetic characterization of
585 vermiculite-based magnetic nanocomposites. *Journal of Non-Crystalline Solids*, **356**, 2574–
586 2577.

587 Tauc, J., Grigorovici, R. & Vancu, A. (1966) Optical Properties and Electronic Structure of
588 Amorphous Germanium. *physica status solidi (b)*, **15**, 627–637.

589 Taylor, H.F.W. (1973) Crystal structures of some double hydroxide minerals. *Mineralogical*
590 *magazine*, **39**, 377–389.

591 Terna, A.D., Elemike, E.E., Mbonu, J.I., Osafire, O.E. & Ezeani, R.O. (2021) The future of
592 semiconductors nanoparticles: Synthesis, properties and applications. *Materials Science and*
593 *Engineering: B*, **272**, 115363.

- 594 Terzis, A., Filippakis, S., Kuzel, H.-J. & Burzlaff, H. (1987) The crystal structure of $\text{Ca}_2\text{Al}(\text{OH})_6\text{Cl}$
595 $\cdot 2\text{H}_2\text{O}$. *Zeitschrift für Kristallographie - Crystalline Materials*, **181**, 29–34.
- 596 Thevenot, F., Szymanski, R. & Chaumette, P. (1989) Preparation and Characterization of Al-Rich
597 Zn-Al Hydrotalcite-Like Compounds. *Clays and Clay Minerals*, **37**, 396–402.
- 598 Tichit, D., Iborra, S., Corma, A. & Brunel, D. (2006) *Base-Type Catalysis. Catalysts for Fine*
599 *Chemical Synthesis*, pp. 171–205. John Wiley & Sons, Ltd.
- 600 Wang, L.-Y., Wu, G.-Q. & Evans, D.G. (2007) Synthesis and characterization of a layered double
601 hydroxide containing an intercalated nickel(II) citrate complex. *Materials Chemistry and*
602 *Physics*, **104**, 133–140.
- 603 Wen, X., Wang, S., Ding, Y., Wang, Z.L. & Yang, S. (2005) Controlled Growth of Large-Area,
604 Uniform, Vertically Aligned Arrays of $\alpha\text{-Fe}_2\text{O}_3$ Nanobelts and Nanowires. *The Journal of*
605 *Physical Chemistry B*, **109**, 215–220.
- 606 Xu, Z.P. & Lu, G.Q. (Max) (2005) Hydrothermal Synthesis of Layered Double Hydroxides (LDHs)
607 from Mixed MgO and Al_2O_3 : LDH Formation Mechanism. *Chemistry of Materials*, **17**,
608 1055–1062.
- 609 Yan, L., Gonca, S., Zhu, G., Zhang, W. & Chen, X. (2019) Layered double hydroxide
610 nanostructures and nanocomposites for biomedical applications. *Journal of Materials*
611 *Chemistry B*, **7**, 5583–5601.
- 612 Zhao, R., Yin, C., Zhao, H. & Liu, C. (2003) Synthesis, characterization, and application of
613 hydrotalcites in hydrodesulfurization of FCC gasoline. *Fuel Processing Technology*, **81**,
614 201–209.

615